Zn sorption modifies dynamically the layer and interlayer structure of vernadite

Sylvain Grangeon [a,*], Alain Manceau [a], Julien Guilhermet [a], Anne-Claire Gaillot [b], Martine Lanson [a], Bruno Lanson [a]

[a] *ISTerre, Université Grenoble 1 – CNRS, F-38041 Grenoble, France*
[b] *Institut des Matériaux Jean Rouxel, CNRS – Université de Nantes, 2 Rue de la Houssinière, BP 32229, 44322 Nantes Cedex 3, France*

Abstract

In surficial environments, the fate of many trace metals is influenced by their interactions with the phyllomanganate vernadite, a nano-sized and turbostratic variety of birnessite. To advance our understanding of the surface reactivity of vernadite, synthetic vernadite (δ-MnO_2) was equilibrated at pH 5 or 7, reacted with dissolved Zn to produce Zn-sorbed δ-MnO_2 with Zn/Mn atomic ratios from 0.003 to 0.156, and characterized structurally. The octahedral layers in the Zn-free vernadite contain on average ~0.15 vacancies, ~0.13–0.06 Mn^{3+} and ~0.72–0.79 Mn^{4+}. The layer charge deficit is compensated in the interlayer by Mn^{3+} bonded over Mn vacancy sites and Na^+ located in the interlayer mid-plane. The average lateral dimension of coherent scattering domains (CSDs) deduced from X-ray diffraction (XRD) modeling is ~5 nm, consistent with that observed by transmission electron microscopy for individual crystals, indicating that the amounts of edge sites can be estimated by XRD. The average vertical dimension of CSDs is ~1 nm, equivalent to 1.5 layers and less than the observed 3–4 layers in the particles. Zinc sorption at pH 5 and 7 on pre-equilibrated vernadite induced crystal dissolution reducing the lateral CSD size ~15–20%. Zinc K-edge extended X-ray absorption fine structure (EXAFS) spectroscopy and XRD show that Zn occurs in the interlayer above vacancies as a triple-corner-sharing surface complex, which is fully tetrahedral at low Zn/Mn ratios and increasingly octahedral at higher ratios. As Zn/Mn increases, the site density of layer Mn^{3+} decreases from 0.13 ± 0.01 to 0.03 ± 0.01 at pH 5 and from 0.06 ± 0.01 to 0.01 ± 0.01 at pH 7, and that of layer vacancies correspondingly increases from ~0.15 to 0.24 and 0.21 at pH 5 and 7, respectively. These changes likely occur because of the preference of Zn^{2+} for regular coordination structures owing to its completely filled third electron shell ($3d^{10}$ configuration). Thus, sorption of Zn into the interlayer causes the departure of layer Mn^{3+}, subsequent formation of new reactive layer vacancies, and an increase in surface area through a reduction in particle size, all of which dynamically enhance the sorbent reactivity. These results shed new light on the true complexity of the reactive vernadite surface, and pose greater challenges for surface-complexation modeling of its sorption isotherms.

1. INTRODUCTION

Vernadite is the environmentally ubiquitous nano-sized and turbostratic variety of the well-crystallized phyllomanganate birnessite. Its formation is considered to be mediated dominantly by biota, because biogenic oxidation is approximately two orders of magnitude faster than heterogeneous oxidation catalyzed by mineral surfaces (Crerar and Barnes, 1974; Tebo et al., 2004; Morgan, 2005). Vernadite can be produced by bacteria (Mandernack et al., 1995; Schulze et al., 1995; Villalobos et al., 2003; Tebo et al., 2004; Toner et al., 2005; Webb et al., 2005; Boonfueng et al., 2009), fungi (Tani et al., 2003; Miyata et al., 2004, 2007; Santelli et al., 2011), and higher-order organisms (Lanson et al., 2008). Biogenic vernadite was reported or inferred to occur in soils and

* Corresponding author. Present address: BRGM, 3 Avenue Claude Guillemin, 45060 Orléans Cedex 2, France. Tel: +33 238 643 511; fax: +33 238 643 032.
  E-mail address: S.Grangeon@brgm.fr (S. Grangeon).

sediments (Hochella et al., 2005a; He et al., 2008; Lanson et al., 2008), freshwater (Bargar et al., 2009), dry and cold deserts (Dorn and Oberlander, 1981; Dorn et al., 1992; Mckeown and Post, 2001), and marine deposits (Crerar and Barnes, 1974; Bodeï et al., 2007).

The crystal structure of vernadite and of its synthetic analog δ-MnO_2 consists of randomly stacked layers of edge-sharing MnO_6 octahedra with a layer-to-layer distance of ~7.2 Å (Giovanoli, 1969; Drits et al., 1997). Octahedral vacancies in the layer and Mn^{4+} substitution by cations of lower valence (e.g. Mn^{3+}, Ni^{2+}, Co^{3+}, or Cu^{2+}; Manceau et al., 1997, 2007a; Silvester et al., 1997; Webb et al., 2005; Villalobos et al., 2006; Peacock and Sherman, 2007; Grangeon et al., 2008; Bargar et al., 2009; Sherman and Peacock, 2010; Zhu et al., 2010a) create a deficit of charge compensated for by interlayer cations. The density of layer vacancies, and hence the reactivity of vernadite with respect to cation sorption (Zhao et al., 2009), can be increased by the reduction of Mn^{4+} and Mn^{3+} to Mn^{2+} by Cr^{3+} (Manceau and Charlet, 1992; Silvester et al., 1995) and by organic molecules and sunlight (Stone and Morgan, 1984a,b; Sunda and Kieber, 1994; Banerjee et al., 1999; Villatoro-Monzón et al., 2003; Pizzigallo et al., 2004; Kwon et al., 2009a; Nasser et al., 2009). Vernadite surface reactivity is reinforced further by its nanometer size, which increases the amounts of border sites relative to birnessite.

The weak undersaturation of surface oxygens caused by the presence of di- and trivalent cations in the octahedral layer is usually balanced by exchangeable hydrated alkaline or alkali earth cations, such as Na^+ and Ca^{2+}, forming outer-sphere complexes in the interlayer (Drits et al., 1998; Lanson et al., 2002a). In contrast, the strong undersaturation of surface oxygens bordering layer vacancies is more permanently balanced by multivalent cations sorbed mainly as triple-corner-sharing surface complexes (TC configuration, Fig. 1; Silvester et al., 1997; Drits et al., 2002; Manceau et al., 2002a; Lanson et al., 2002b; Jurgensen et al., 2004; Li et al., 2004; Webb et al., 2005; Peacock and Sherman, 2007; Peacock, 2009; Kwon et al., 2010; Peña et al., 2010; Zhu et al., 2010b). The deficit of layer charge may also be balanced partly by the formation of double-corner-sharing and triple-edge-sharing surface complexes (DC and TE configurations, respectively, Fig. 1; Lanson et al., 2002b; Manceau et al., 2002a, 2007a; Kwon et al., 2010).
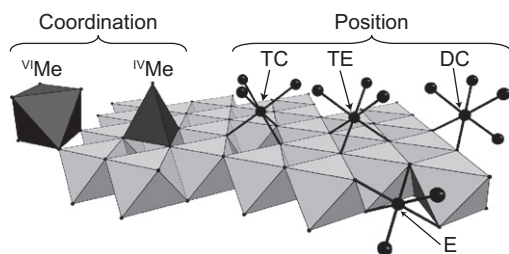
As a result of both its ubiquity and high surface reactivity, vernadite is often associated with transition metals, including Zn, rare-earth elements, and actinides in surface, subsurface, and marine environments, such as in ferromanganese crusts, nodules and grain coatings (Ostwald and Frazer, 1973; Mckenzie, 1980; Aplin and Cronan, 1985; Chukhrov et al., 1985; Bogdanov et al., 1995; Koschinsky and Halbach, 1995; Lei and Boström, 1995; Friedl et al., 1997; Duff et al., 1999; Exon et al., 2002; Koschinsky and Hein, 2003; Manceau et al., 2003, 2004, 2007a,b; Marcus et al., 2004a; Hochella et al., 2005b; Isaure et al., 2005; Bodeï et al., 2007; Peacock and Sherman, 2007; Takahashi et al., 2007; Vaněk et al., 2008; Bargar et al., 2009). Phyllomanganates have been reported to influence Zn mobility also in wetlands (Olivie-Lauquet et al., 2001), in areas affected by atmospheric fallout from smelting activities (Manceau et al., 2000), and in the hyporheic zone of rivers contaminated by mining operations (Fuller and Harvey, 2000). Laboratory experiments indicate that when Zn, and other metals such as Ni, are introduced into a bacteria-rich medium with microbially produced vernadite and biofilms, sorption predominantly occurs on vernadite (Toner et al., 2006; Peña et al., 2010, 2011; Zhu et al., 2010b), consistent with its close association with trace metals in natural systems.

Previous structural studies of Zn sorption on synthetic hexagonal birnessite containing ~0.17 vacancy and ~0.11 layer Mn^{3+} per octahedral layer site (E site, Fig. 1) showed that Zn coordination varies with surface loading: Zn is dominantly tetrahedral at low Zn/Mn atomic ratios ($^{IV}Zn/^{VI}Zn \approx 2$ for Zn/Mn ≈ 0.008), and octahedral at higher Zn loading (Drits et al., 2002; Manceau et al., 2002a; Lanson et al., 2002b). Recent quantum mechanical calculations suggested that ^{VI}Zn is stabilized by H-bonding between neighboring H_2O molecules located near the interlayer mid-plane and belonging to the coordination spheres of two Zn^{2+} cations each adsorbed on one side of the interlayer space (Kwon et al., 2009b). If this is the case, the $^{IV}Zn/^{VI}Zn$ ratio should vary not only with the surface coverage, but also with the layer stacking order because disruption of the layer periodicity should hinder the formation of H-bonds. To verify this hypothesis, two series of δ-MnO_2 were equilibrated at pH 5 and 7, then equilibrated with Zn solutions to achieve a final solid Zn/Mn mole ratio of 0.003–0.156, and characterized structurally. Interest was further whetted by the finding from X-ray diffraction (XRD) simulations that the density of Mn^{4+} vacancies increased and the layer size decreased with increasing Zn loading. Thus, the crystal chemistry of Zn at the surface of vernadite appeared to be influenced by the stacking order of the sorbent, while the defective structure of the phyllomanganate layers was in return modified dynamically by Zn.

2. MATERIALS AND METHODS

2.1. Sample synthesis and zinc sorption protocol

δ-MnO_2 was synthesized using stoichiometric amounts of $KMnO_4$ and $MnCl_2$ as described by Villalobos et al. (2003). Two suspensions were prepared at $I = 0.1$ M $NaNO_3$ using ~1.5 g L^{-1} of δ-MnO_2 powder and deionized

Fig. 1. Possible inner-sphere cation complexes at the δ-MnO_2 surface. Octahedral and tetrahedral coordinations are represented as closed polyhedra (left) and sorption sites as ball-and-sticks (right). DC, TC, TE and E refer to double-corner sharing, triple-corner sharing, triple-edge sharing interlayer sites and octahedral layer sites, respectively.

water (resistivity > 18 MΩ cm^{-1}), which was boiled and degassed by bubbling argon for 30 min before use. One batch was equilibrated at pH 5.0 ± 0.1 and another at pH 7.0 ± 0.2 ($T = 25$ °C). Zinc was introduced next by dropwise addition (0.2–1.0 mL min^{-1} depending on the Zn/Mn ratio) with intense stirring of 5.0×10^{-3} M (pH 5) and 5.0×10^{-4} M (pH 7) Zn(NO$_3$)$_2$ solutions. Solution concentrations were chosen to maximize the concentration of free aqueous Zn^{2+} while avoiding metal precipitation, and their volumes varied to obtain the desired Zn/Mn ratios. Ionic strength and pH were kept constant during the addition of Zn(NO$_3$)$_2$. Finally, the pH was re-adjusted after the last addition of Zn(NO$_3$)$_2$ solution until fully stabilized (usually for ~12 h). Then samples were filtered, rinsed with deionized water, and freeze-dried. Sample codes are ZnXdBiY, where X stands for the pH and Y for the atomic ratio of Zn to Mn (Table 1).

2.2. Chemical analysis

Total Mn, Na and Zn contents were measured by Inductively Coupled Plasma – Atomic Emission Spectrometry (ICP-AES, Perkin-Elmer Optima 3000) on aliquots of solutions obtained from ~5 mg Mn oxide digested in ~15 mL NH$_3$OHCl (0.7 mol L^{-1}, pH 1.9). Average Mn oxidation states were measured in triplicate by potentiometric titration, using (NH$_4$)$_2$FeSO$_4$ (Mohr salt) and Na$_4$P$_2$O$_7$ (Table 1; Lingane and Karplus, 1946; Vetter and Jaeger, 1966; Gaillot, 2002). This method requires only the measurement of three equivalence volumes (see Supplementary information) to provide a fast, accurate, and robust estimate of this parameter. In contrast, titration methods using potassium or sodium iodide (Murray et al., 1984; Villalobos et al., 2003), sodium oxalate (Freeman and Chapman, 1971; Silvester et al., 1997; Villalobos et al., 2003), or oxalic acid (Feng et al., 1992) require the accurate determination of both sample mass and concentrations of titrating solutions. Additional uncertainties come from the analytical determination of the amount of Mn^{2+} resulting from the reductive dissolution of the phyllomanganate.

2.3. EXAFS spectroscopy

All EXAFS spectra, including previously acquired reference spectra (Marcus et al., 2004a), were collected on beam-line 10.3.2 at the Advanced Light Source (Berkeley, USA; Marcus et al., 2004b). Because Zn can be tetrahedral and octahedral at medium to high Zn/Mn ratio and EXAFS spectra represent the weighted average of all bonding environments of the target element, the fraction of each coordination species was determined by linear combination fitting of chalcophanite as ^{VI}Zn reference (ZnMn$_3$O$_7$.3H$_2$O; Wadsley, 1955; Post and Appleman, 1988), and ^{IV}ZndBi from a marine ferromanganese nodule of Baltic Sea as ^{IV}Zn reference (Marcus et al., 2004a). Zinc is sorbed at vacancy sites in both references. It is fully octahedral in chalcophanite (Post and Appleman, 1988; Manceau et al., 2002a), and fully tetrahedral, within the 7% precision, in ^{IV}ZndBi (Marcus et al., 2004a). Spectra were reconstructed in $k^3\chi(k)$ space initially with one component, and the regression evaluated over the 1.8–10.6 Å^{-1} k range with the normalized sum-squared residual $NSS = \Sigma(k^3\chi_{exp} - k^3\chi_{cal})^2/\Sigma(k^3\chi_{exp})^2$. A second component was considered statistically significant if NSS decreased by at least ~10% and if its fractional contribution was >10% (e.g. Manceau et al., 2000, 2002b; Isaure et al., 2002). The weights of reference spectra in the linear fits to the data were the only adjustable parameters. The sum of ^{VI}Zn and ^{IV}Zn species was not constrained to 1, but should be close to this value if the local environment of Zn is well described with the end-members for octahedral and tetrahedral Zn.

2.4. Powder XRD

XRD patterns were collected on a Bruker D5000 diffractometer, equipped with a SolX solid-state detector (Baltic Scientific Equipments) and CuKα radiation ($\lambda = 1.5418$ Å), over the 5–80 °2θ angular range (17.6–1.2 Å) with 40 s counting time per 0.04 °2θ step. Usual structure refinement methods such as the Rietveld method are inapplicable because of the turbostratic stacking of vernadite (100% of random stacking faults). Simulations were performed using the formalism described by Drits and Tchoubar (1990), and successfully applied previously to both natural and synthetic phyllomanganates (see for example Chukhrov et al., 1985; Manceau et al., 1997; Drits et al., 1998; Lanson et al., 2000, 2002b; Gaillot et al., 2005, 2007; Villalobos et al., 2006; Grangeon et al., 2008, 2010).

The layer and interlayer structure (nature, position and quantity of layer and interlayer species) and the dimension

Table 1
Chemical composition of Zn-sorbed δ-MnO$_2$ expressed as atomic ratios.

Sample	Zn/Mn	Na/Mn	Mn ox. degree[a]	Layer Mn^{3+},[b]
Zn5dBi03	0.0032 ± 0.0013	0.2417 ± 0.0024	3.76 ± 0.01	0.13 ± 0.01
Zn5dBi13	0.0132 ± 0.0043	0.2563 ± 0.0068	3.79 ± 0.01	N.D.[c]
Zn5dBi61	0.0613 ± 0.0024	0.2207 ± 0.0040	3.79 ± 0.01	0.12 ± 0.01
Zn5dBi153	0.1531 ± 0.0012	0.0784 ± 0.0012	3.85 ± 0.01	0.03 ± 0.01
Zn7dBi03	0.0030 ± 0.0018	0.3153 ± 0.0025	3.83 ± 0.02	0.06 ± 0.01
Zn7dBi11	0.0108 ± 0.0043	0.3375 ± 0.0087	3.83 ± 0.01	N.D.[c]
Zn7dBi53	0.0531 ± 0.0020	0.2841 ± 0.0039	3.83 ± 0.01	0.06 ± 0.01
Zn7dBi156	0.1555 ± 0.0021	0.1624 ± 0.0021	3.88 ± 0.01	0.00 ± 0.02

[a] Standard errors calculated from triplicates (Webster, 2001).
[b] Layer Mn^{3+} calculated from the average oxidation degree and the amount of interlayer Mn deduced from XRD.
[c] Not determined because the XRD patterns are similar to Zn5dBi03/Zn7dBi03.

of coherent scattering domains (CSDs) in the **a**–**b** plane were determined first from the simulation of the high-angle region (30–80 °2θ) dominated by *hk* diffraction bands, *hkl* reflections being unresolved owing to sample turbostratism. The *hk* bands at 2.42 Å, 1.41 Å and 1.22 Å were indexed as $11,20$, $31,02$ and $22,40$ with a C-centered unit cell. The *a* and *b* parameters were calculated from the position of the $31,02$ band (Grangeon et al., 2008), which is essentially insensitive to other structural parameters. These parameters were obtained from the simulation of the high-angle tail of the $11,20$ band (Villalobos et al., 2006; Drits et al., 2007; Grangeon et al., 2008; Lanson et al., 2008). Atomic positions were considered to be invariant among samples, and Na to be coordinated always to three water molecules, to reduce the number of adjustable parameters (Post and Veblen, 1990; Villalobos et al., 2006; Grangeon et al., 2008).

The average number of layers stacked coherently in diffracting crystallites was determined next from the simulation of the low angle-region (5–30 °2θ) which contains basal $(00l)$ reflections. The CSD size along the **c*** axis was optimized, while keeping all other structural parameters to their optimal values derived from the simulation of the high-angle region. Fit quality was evaluated with the usual R_{wp} and Goodness of Fit ($GoF = R_{wp}^2/R_{exp}^2$) factors (Howard and Preston, 1989). The trial-and-error approach used here by necessity prevents the calculation of a covariance matrix. The precision on parameter values obtained from the simulation of turbostratic phyllomanganates, was estimated previously (Villalobos et al., 2006; Drits et al., 2007; Grangeon et al., 2008; Lanson et al., 2008). The uncertainty on the *b* lattice parameter is ± 0.001 Å (Grangeon et al., 2008), and the uncertainty on the sum of DC and TC site occupancy is ± 0.01 atom per octahedral site. Note that diffraction does not allow the differentiation of DC and TC complexes, because their positions are crystallographically equivalent (Grangeon et al., 2008). When CSDs include 2–4 layers, as in vernadite, the precision from XRD on their size is likely better than 0.2 layer, a fivefold intensity increase being observed for the 001 reflection when the average number of layers in CSDs increases from 2.1 to 3.4 (Grangeon et al., 2010). The precision of the CSD size in the **a**–**b** plane is estimated to $\pm 10\%$. The sensitivity of XRD to this parameter was demonstrated in Fig. 6 of Villalobos et al. (2006), which shows that reducing the CSD size from 60 to 30 Å dramatically modifies the XRD profile.

2.5. Transmission electron microscopy

Transmission electron microscopy (TEM) images were acquired on a Hitachi H9000 NAR microscope equipped with a LaB_6 cathode, operated at 300 kV, and a Multiscan GATAN charge-coupled device (CCD) camera. Highly diluted aqueous suspensions of the samples were dried on a copper mesh grid covered with a 20 nm thick holey carbon membrane. The extremely limited dimensions of individual particles restrained their observation above the carbon membrane.

3. RESULTS

3.1. Chemical analysis

The average Mn oxidation state is between 3.76 ± 0.01 (Zn5dBi03) and 3.88 ± 0.01 (Zn7dBi156) instead of nominally 4.0 for stoichiometric δ-MnO_2, meaning that all samples contain mixed-valent states of Mn (Table 1). Low-valence Mn may substitute for Mn^{4+} in δ-MnO_2 layers (Mn^{3+} only) or be sorbed at vacancy sites (Mn^{2+} and Mn^{3+}; see for example Jurgensen et al., 2004; Tebo et al., 2004; Webb et al., 2005; Toner et al., 2006; Villalobos et al., 2006). It was concluded from the interlayer Mn–O bond length [$d(^{DC/TC/TE}$Mn–O)] derived from XRD that the interlayer does not contain Mn^{2+} (Grangeon et al., 2010). In the two pH series, the average oxidation state was 0.05 ± 0.02 higher and the amount of Na lower at high Zn/Mn ratio (Zn5dBi153 and Zn7dBi156). This variation suggests that Zn replaces both Mn^{3+} and interlayer Na^+, at least at high loading.

3.2. EXAFS spectroscopy

At low Zn/Mn ratio and pH 5 (Zn5dBi13), the EXAFS spectrum is nearly identical to that of the ^{IV}Zn reference (Fig. 2). At intermediate (Zn5dBi61) and even more so at high (Zn5dBi156) Zn/Mn ratio, a shoulder appears at $k \approx 3.8$ Å^{-1} and the splitting of the second oscillation at $k \approx 6.1$ Å^{-1} becomes less deep. Linear combination fits to both spectra indicate that the relative contributions of the ^{IV}Zn and ^{VI}Zn coordination species are about $(89 \pm 10)\%$
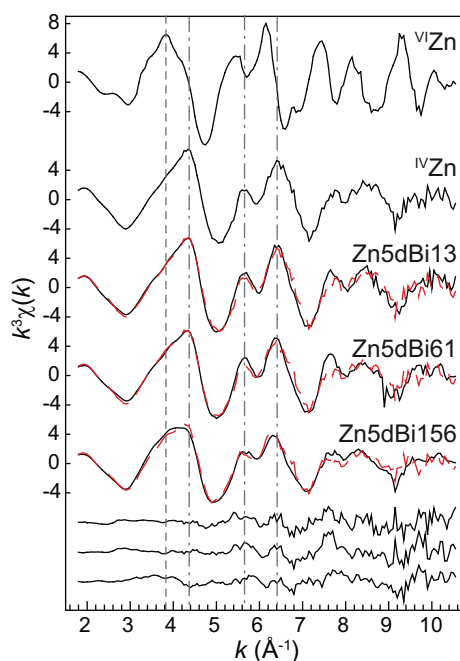

Fig. 2. Zn-K-edge EXAFS spectra of Zn5dBi13, Zn5dBi61 and Zn5dBi156 (solid lines) with their best simulations overlaid (dashed lines). The spectra of the ^{VI}Zn (chalcophanite) and ^{IV}Zn (^{IV}Zn-sorbed vernadite) references are shown on top. Fitting residuals are shown at the bottom. Zn5dBi03 was too diluted to measure a good quality spectrum.
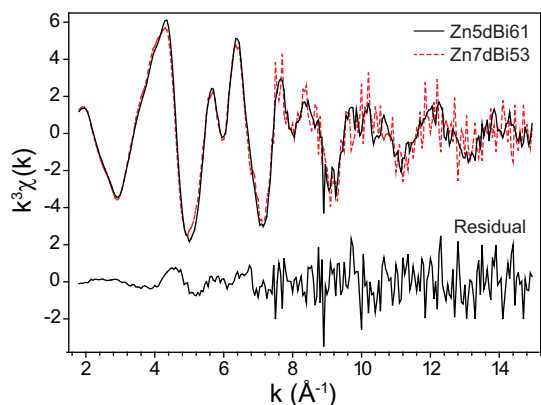
Fig. 3. Zn-K-edge EXAFS spectra of Zn5dBi61 (solid line) and Zn7dBi53 (dashed line), with difference at the bottom.

and $(14 \pm 10)\%$ for Zn5dBi61, and about $(73 \pm 10)\%$ and $(26 \pm 10)\%$ for Zn5dBi156. The high quality of the reconstructions indicates that the bonding environment of Zn can be described as a binary mixture of Zn sorbed in DC/TC configuration (Fig. 1), apparently on the same type of surface site, but with two coordinations, tetrahedral at low surface coverage then octahedral. The EXAFS spectra at medium Zn concentration are statistically indistinguishable at pH 5 and 7 (Zn5dBi61 and Zn7dBi53, Fig. 3), and thus fitted with the same proportions of ^{IV}Zn and ^{VI}Zn. Because Zn5dBi61 corresponds to a mixture of ^{IV}Zn and ^{VI}Zn bonding environments, this spectral similarity suggests that the relative contribution of each complex is essentially independent of pH. This hypothesis is confirmed below by XRD.

3.3. Qualitative description of XRD patterns

3.3.1. Layer symmetry and Mn^{3+} content

The XRD patterns (Fig. 4) show only broad basal reflections and asymmetric hk bands characteristic of δ-MnO$_2$ (Giovanoli, 1980; Drits et al., 2007). The ratio of the peak positions measured for the 11,20 and 31,02 bands ($\sim$1.72) is close to $\sqrt{3}$ and the 31,02 band is nearly symmetrical, which is indicative of hexagonal layer symmetry (Drits et al., 2007). Despite the sixfold layer symmetry, the structure will be described with a C-centered orthogonal unit cell and $a = \sqrt{3} \times b$ for consistency with previous structural studies of phyllomanganates. The b dimension is 2.840 ± 0.002 Å, indicative of a low Mn^{3+} content in the hexagonal layer ($\sim$0.00–0.10 per layer octahedron; Villalobos et al., 2006; Grangeon et al., 2008; Lanson et al., 2008). In comparison, lithiophorite, which contains 32% layer Mn^{3+} (Manceau et al., 2005), has a b dimension of 2.925 Å (Post and Appleman, 1994).

3.3.2. Structural evolution with Zn loading

The width and amplitude of the 001 and 002 reflections are similar for all samples, thus the CSD dimension in the c^* direction is independent of the Zn/Mn ratio and pH. From the broadening of basal reflections, the diffracting crystallites contain approximately 1.5 layers on average, therefore

many constitutive layers from the δ-MnO$_2$ nanoparticles are either monodispersed, not strictly parallel, or parallel but not spaced regularly (Fig. 4; Lanson et al., 2008). The two lowest Zn/Mn patterns are similar at pH 5 (Zn5dBi03 and Zn5dBi13) and pH 7 (Zn7dBi03 and Zn7dBi11) with a scattering tail that decreases almost monotonically from 40 to 60 $^\circ 2\theta$. A dip at $\sim$47 $^\circ 2\theta$ followed by a hump at $\sim$52 $^\circ 2\theta$ are clearly observed for Zn5dBi61 and Zn7dBi53 and become more prominent at highest Zn loading. This evolution is a signature of increasing amounts of high-Z atoms in DC/TC configuration (Villalobos et al., 2006; Drits et al., 2007; Grangeon et al., 2008; Lafferty et al., 2010), consistent with EXAFS results.

3.4. XRD modeling

The XRD simulations are shown in Fig. 5 and results summarized in Tables 2 and 3. The model structures for low-Zn δ-MnO$_2$ are close at pH 5 and 7. At low Zn loading, the layers have $\sim$0.15 vacancy per octahedral site, and the deficit of charge is approximately equally compensated for by $^{DC/TC}Mn^{3+}$ ($0.085 \times 3+$) and Na$^+$ ($0.24/0.30 \times 1+$). The best model was obtained by adding 0.01–0.02 Mn above the tridentate cavities formed by three layer octahedra (TE position, Fig. 1). EXAFS spectroscopy did not allow differentiation of the relative contributions of ^{DC}Mn and ^{TC}Mn nor confirmation of the presence of ^{TE}Mn owing to the multiplicity of Mn sites having similar local environments (DC, TC, TE, E sites), and in particular a similar first oxygen shell. The average $^{DC/TC}Mn$–O and ^{TE}Mn–O distances are $\sim$2.05 Å, which supports the conclusion that interlayer Mn is trivalent based on bond valence calculations (for more details, see Grangeon et al., 2010).

The density of layer vacancies is $\sim$0.10 (pH 5) and $\sim$0.05 (pH 7) higher at high Zn content than at low Zn content, values that match the decrease in the number of layer Mn^{3+} (0.10 and 0.06, respectively, Table 1). At medium and high loading, Zn remains sorbed at DC/TC sites dominantly in tetrahedral coordination, with the proportion of octahedral Zn increasing from $\sim$17–20% to 27–33% at medium and high loading, respectively, in agreement with EXAFS data modeling that indicates an increase from 14 to 26%. The amount of interlayer Mn does not follow a regular pattern, decreasing first at intermediate loading then increasing again at high loading. With increasing Zn, the CSD dimension decreases steadily from $\sim$5.5 to $\sim$4.5 nm in the layer plane and remains constant perpendicular to this plane ($\sim$1 nm).

3.5. Textural evolution

Under the TEM, aggregated crystals have a mean diameter of $\sim$10 nm with a few visible euhedral hexagons (Fig. 6a and b). Observation of isolated crystals at higher resolution confirms a mean diameter of 5–10 nm (Fig. 6c), consistent with the CSD sizes of 5–6 nm in the **a**–**b** plane (Table 2), and shows that the layers are frequently curled (Fig. 6d), leading to a loss of periodicity in the **a**–**b** plane. Crystal aggregation did not allow confirmation of the 0.8–1.1 nm reduction of CSD size with Zn loading (Table 2).
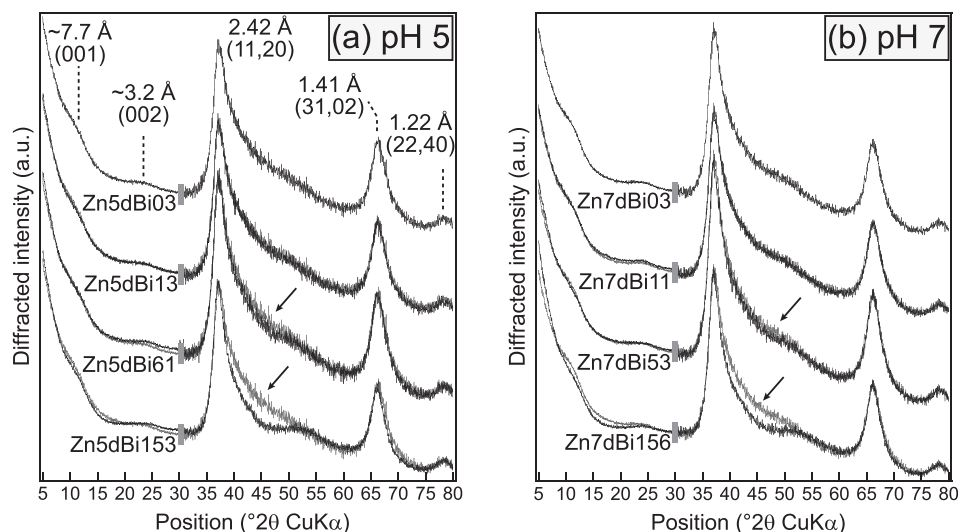
Fig. 4. XRD patterns of Zn-sorbed δ-MnO₂. (a) pH 5, (b) pH 7. The high-angle regions on the right side of the grey bars were scaled by a factor 5. In each series, the sample with the lowest Zn/Mn ratio is shown as a light grey line to emphasize the evolution of the XRD traces with Zn content (arrows).
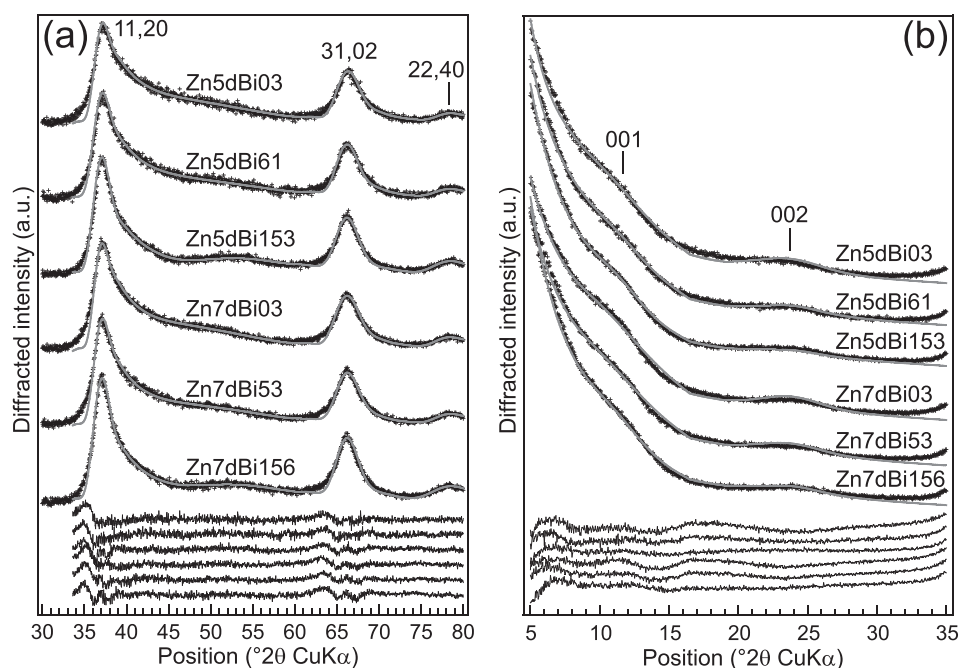

Fig. 5. Simulations of the XRD patterns for Zn-sorbed δ-MnO₂. (a) 11,20, 02,31, and 22,40 scattering bands. (b) 00l basal reflections. Black crosses are experimental data, solid overplots are calculated profiles, and solid blacklines at the bottom are difference plots. Parameters used for the simulations are listed in Tables 2 and 3.

Along the c^* axis, crystals appear to be composed of ~3–4 layers (Fig 6d), compared to mean CSD sizes of ~1.5 layers (Table 2).

4. DISCUSSION

4.1. Relation between CSD size and physical particle size

Turbostratic phyllomanganates have CSD sizes in the nanometer range, both in and perpendicular to the layer plane (Jurgensen et al., 2004; Villalobos et al., 2006; Grangeon et al., 2008, 2010; Lanson et al., 2008; Bargar et al., 2009). There is no evidence yet that these domain sizes are close in value to the actual particle sizes. Aggregation of crystallites, with slight rotations or translations between them, commonly leads to CSD sizes in the **a**–**b** plane smaller than particle sizes (Drits and Tchoubar, 1990). Determining whether CSD sizes are good estimates of particle sizes is however crucial to the quantification and modeling of vernadite reactivity. A key issue is the importance of border
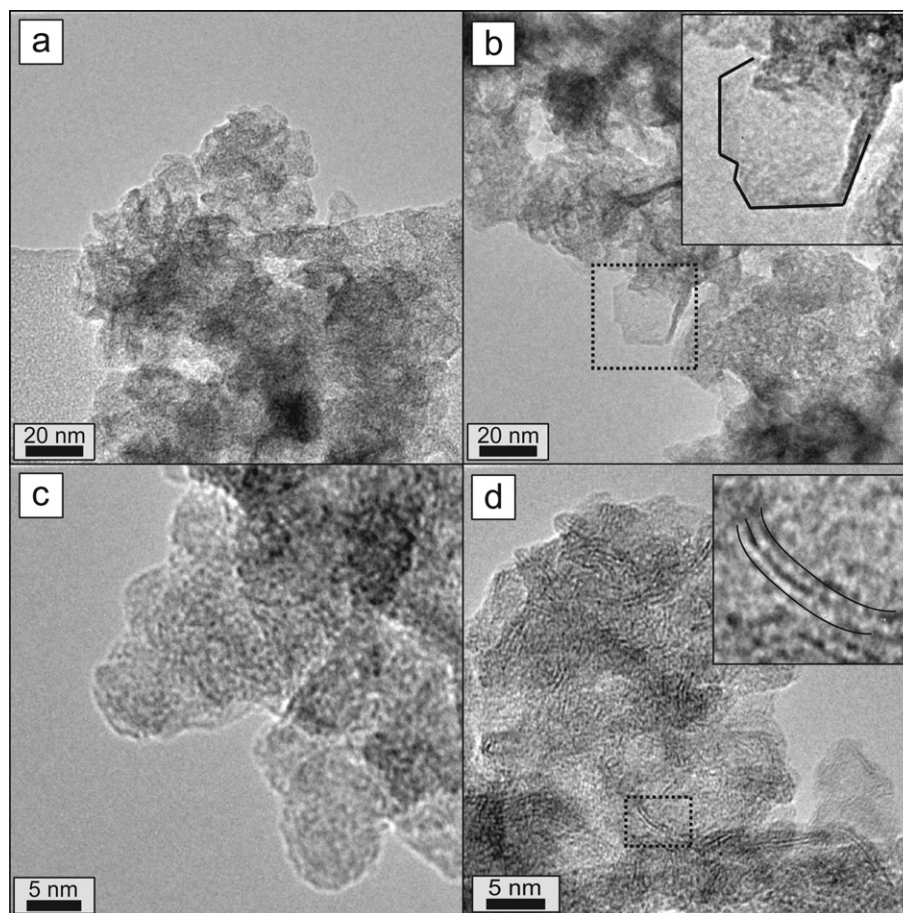
Fig. 6. Electron micrographs of Zn-sorbed δ-MnO₂. (a) Overview of Zn5dBi156. (b) View of a hexagonal shaped Zn5dBi03 crystal. (c) Detailed view of Zn5dBi156 crystals. (d) Lattice fringe images of Zn5dBi03 crystals with the electron beam parallel to the layers.

sites which becomes paramount when the lateral dimension of the phyllomanganate layer is extremely small, as in the present case (Webb et al., 2005).

The agreement between TEM (5–10 nm) and XRD (5–6 nm) is quite good in the **a–b** plane. The lower XRD figure comes in part from the structural strain induced by the curling of the layers. Along the c^* direction, the agreement between TEM (~3–4 layers) and XRD (~1.5 layers) is, however, less good. The difference may be explained by a variation of the radius of curvature of the bent layers, which modifies locally the layer-to-layer distance, leading to a loss in the coherence of the diffracted X-rays. This basal distance also depends on the layer charge and its compensation by interlayer species, which have no reason to be homogenous within a given manganese layer and hence across the interlayer space.

4.2. Zinc coordination

Atomic coordinates of the layer and interlayer species in Zn-sorbed δ-MnO₂ are consistent with those reported previously for natural and synthetic phyllomanganates (see for example Drits et al., 1997; Manceau et al., 1997, 2002a; Lanson et al., 2002b, 2008; Villalobos et al., 2006;

Gaillot et al., 2007; Grangeon et al., 2008). Although Zn is always sorbed at DC/TC sites, its coordination varies with the Zn/Mn ratio: it is exclusively tetrahedral at Zn/Mn $<\sim0.05$ and increasingly octahedral at higher surface loading, consistent with previous reports (Manceau et al., 2002a; Toner et al., 2006; Boonfueng et al., 2009). At similar loading, [VI]Zn is about two times more abundant in Zn-sorbed birnessite, the 3D-ordered variety of vernadite having thicker and larger crystals (Fig. 7; Manceau et al., 2002a; Lanson et al., 2002b). Geometry optimization based on density functional theory showed that [VI]Zn is stabilized by electrostatic interactions between water molecules bonded to two neighboring $Zn(O,H_2O)_6$ octahedra in the interlayer, each attached to a distinct layer (Kwon et al., 2009b), in agreement with structural studies (Drits et al., 2002; Manceau et al., 2002a; Lanson et al., 2002b). These interactions should be weaker in the interlayer of two incoherently stacked and laterally small layers, as it is the case for δ-MnO₂. More generally, the higher abundance of defects in phyllomanganate nanoparticles likely favors [IV]Zn, because this complex compensates the charge deficits from the unsaturated surface oxygens at Mn vacancies more effectively than does [VI]Zn (Manceau et al., 2002a; Kwon et al., 2009b).

Table 2
Crystal data.

Sample	a (Å)	b (Å)	d (0 0 1) (Å)	Average CSD size (nm)		R_{wp} (%)[b]	GoF (%)[b]
				In the **a**–**b** plane[a]	Along the **c*** axis		
Zn5dBi03	4.919	2.840	7.2	5.4	1.1	5.25–6.99	9.24–5.05
Zn5dBi61	4.922	2.842	7.2	4.7	1.1	3.53–5.97	4.25–3.89
Zn5dBi153	4.915	2.838	7.2	4.6	1.1	2.92–4.56	3.07–2.53
Zn7dBi03	4.929	2.846	7.2	5.8	1.1	4.37–6.82	6.41–5.22
Zn7dBi53	4.922	2.842	7.2	5.2	1.1	3.84–5.99	5.05–4.03
Zn7dBi153	4.915	2.838	7.2	4.7	1.2	3.52–4.63	4.66–2.82

[a] The CSD size in the **a**–**b** plane is expressed as the mean diameter of disk-shaped domains.
[b] Calculated over the low- and high-angle regions, respectively.

Table 3
Atomic coordinates and site occupancies of Zn-sorbed vernadite.

Atom	x[a]	y	z	Occ[b] Zn5dBi03	Occ Zn5dBi61	Occ Zn5dBi153	Occ Zn7dBi03	Occ Zn7dBi53	Occ Zn7dBi156
^{E}Mn (Mn1)[c]	0.000	0.000	0.000	0.860	0.860	0.760	0.845	0.830	0.790
O_{Mn1}	0.333	0.000	0.139	2.000	2.000	2.000	2.000	2.000	2.000
$^{DC/TC}$Mn (Mn2)[d]	0.000	0.000	0.299	0.085	0.065	0.120	0.085	0.080	0.100
O_{Mn2}	−0.333	0.000	0.472	0.255	0.195	0.360	0.255	0.240	0.300
^{TE}Mn (Mn3)	−0.333	0.000	0.299	0.020	0.010	0.000	0.020	0.015	0.000
O_{Mn3}	0.000	0.000	0.472	0.060	0.030	0.000	0.060	0.045	0.000
^{IV}Zn (Zn1)	0.000	0.000	0.246	0.000	0.050	0.110	0.000	0.040	0.100
O_{Zn1}	0.000	0.000	0.514	0.000	0.050	0.110	0.000	0.040	0.100
^{VI}Zn (Zn2)	0.000	0.000	0.306	0.000	0.010	0.040	0.000	0.010	0.050
O_{Zn2}	−0.333	0.000	0.472	0.000	0.030	0.120	0.000	0.030	0.150
Na^+	−0.500	0.000	0.500	0.080	0.067	0.030	0.100	0.090	0.050
Na^+	−0.250	0.250	0.500	0.080	0.067	0.030	0.100	0.090	0.050
Na^+	−0.250	−0.250	0.500	0.080	0.067	0.030	0.100	0.090	0.050
O_{Na+}	0.190	0.000	0.500	0.240	0.200	0.090	0.300	0.270	0.150
O_{Na+}	−0.095	0.285	0.500	0.240	0.200	0.090	0.300	0.270	0.150
O_{Na+}	−0.095	−0.285	0.500	0.240	0.200	0.090	0.300	0.270	0.150

Note: Symmetry operations: (x, y, z), $(−x, −y, −z)$, $(x + ½, y + ½, z)$, $(−x + ½, −y + ½, −z)$. The $C2/m$ space group can be used to represent the structure model. However, care has to be taken to not generate equivalent positions from adjacent layers because δ-MnO_2 has no 3D periodicity.
[a] Atomic coordinates x, y, z are expressed as fractions of the a, b and d_{001} parameters, respectively.
[b] Occupancies are given per half unit cell (i.e., per octahedral layer site), and as the sum of the (x, y, z) and $(−x, −y, −z)$ equivalent sites.
[c] Atomic sites (E, TC, TE) and coordinations (IV, VI) are schematized in Fig. 1. The Debye–Waller thermal factors (B) were fixed to 0.5 Å^2 for Mn1, 1.0 Å^2 for O1, 2.0 Å^2 for O6 and K$^+$, and 1.5 Å^2 for the other species.
[d] DC and TC sites are undistinguishable by XRD in such disordered structures owing to their similar atomic coordinates (Grangeon et al., 2008).

4.3. Modification of vernadite structure and reactivity with metal sorption

The density of vacant sites on synthetic vernadite is considered usually to be invariant at constant pH with the metal loading in the interlayer (e.g. Tonkin et al., 2004; Villalobos et al., 2005; Zhao et al., 2009; Zhu et al., 2010b). Results from this study show that the crystal size, density of layer vacancies, and redox properties (i.e., layer Mn^{3+}/Mn^{4+} ratio) of vernadite, hence its sorption capacity and surface reactivity, evolve dynamically with Zn sorption over vacancy sites (Fig. 8). The density of sorption sites increases both as a result of a reduction of the CSD dimension in the **a**–**b** plane and an increase of the number of layer vacancies, this number being anti-correlated, within uncertainties, to layer Mn^{3+} (Table 1). These profound

transformations of the sorbent structure and chemistry are likely irreversible.

Mechanistically, Zn replaces interlayer Na^+ and Mn^{3+} when entering the structure, as reported previously for Pb (Zhao et al., 2009). In addition, it expels layer Mn^{3+}, thus creating new layer vacancies and catalyzing the sorption process. This second effect is detected by XRD at high loading of sorbed Zn, but may occur also at low loading, where the XRD technique is insensitive to small changes in layer site occupancies. Layer Mn^{3+} may be released to solution or instead may disproportionately release Mn^{2+} to solution (Silvester et al., 1997). The driving force for the decrease of layer Mn^{3+} could be the 3d^{10} electronic configuration of Zn that favors regular coordinations (octahedral or tetrahedral), that cannot be achieved when surface oxygens around a vacancy site are bonded to a Mn^{3+} octahedron distorted
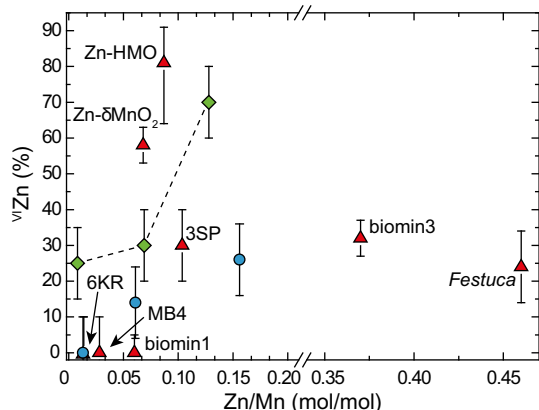
Fig. 7. Fraction of ^{VI}Zn to total Zn sorbed on phyllomanganate as a function of Zn loading. Solid circles: this study; solid triangles: previous studies on vernadite; solid diamonds: previous studies on birnessite. MB4 is from a marine nodule (Marcus et al., 2004a), 3SP and 6KR are from quartz-coatings (Manceau et al., 2007a), *Festuca* was produced by the graminaceous *Festuca rubra* (Lanson et al., 2008), biomin1 and biomin3 by the bacterial strain *Pseudomonas* (Toner et al., 2006), Zn-δMnO_2 (Toner et al., 2006) and Zn-HMO (Boonfueng et al., 2006) are synthetic samples. Birnessite data are from Lanson et al. (2002b) and Manceau et al. (2002a). Birnessite is a 3D-ordered phyllomanganate and vernadite a turbostratic phyllomanganate.
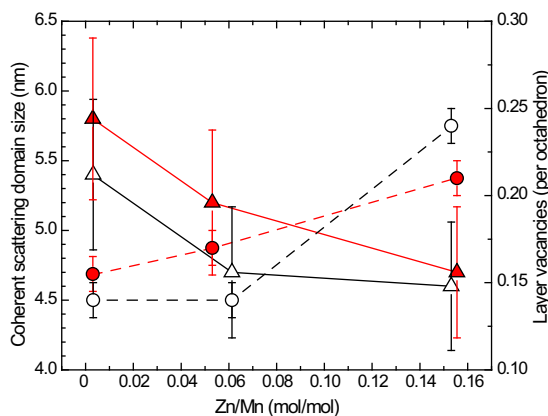

Fig. 8. Evolution of coherent scattering domain sizes in the **a–b** plane (triangles) and layer vacancies (circles) as a function of Zn/Mn ratio for Zn-sorbed δ-MnO_2 prepared at pH 5 (open symbols) and 7 (solid symbols).

by the Jahn–Teller effect (Manceau et al., 2002a). At highest loading, $^{DC/TC}Mn$ increased though, perhaps because of retention of Mn^{3+} in the interlayer or re-adsorption of excess aqueous Mn produced by the dissolution of the nanoparticles at their edges, as suggested by the strong reduction of the CSD size (Table 2). With an initial CSD diameter of 54–58 Å in the **a–b** plane, this ~15–20% reduction increases by ~0.03 the number of border sites available for Zn sorption (Webb et al., 2005), this effect remaining minor compared to layer vacancy creation.

The reduction of the CSD size and the increasing number of layer vacancies with Zn loading do not have the same

dependence on pH. At pH 5 and 7, the density of layer vacancies remained equal to 0.14–0.17 per octahedral site at low and medium surface coverage and increased to 0.21–0.24 at high surface coverage (Table 3). In contrast, the CSD size decreased from low to medium surface coverage and remained stable from medium to high surface coverage at pH 5, whereas it continuously decreased at pH 7 (Table 2).

4.4. Concluding remarks

The observed modification of the phyllomanganate layer structure by surface complexation of a metal over vacancy sites from the MnO_2 layer is reported for the first time in this paper. According to the current paradigm, hydrolyzable cations had to penetrate into layer vacancies to change the layer composition and structure. This process reduces the layer charge by two valence units when Ni^{2+} or Cu^{2+} are incorporated into a Mn^{4+} vacancy (Manceau et al., 2007a; Peacock and Sherman, 2007; Sherman and Peacock, 2010). However, it may also increase, not necessarily decrease, the sorbent reactivity by reductive dissolution of the manganese layer through the oxidation of Co^{2+} to Co^{3+} or Cr^{3+} to Cr^{6+} with electron transfer to Mn^{3+}/Mn^{4+} and the subsequent release into solution of Mn^{2+} (Manceau and Charlet, 1992; Silvester et al., 1995; Manceau et al., 1997). The new type of metal–vernadite interaction described here is an additional source of complexity for the meaningful interpretation and modeling of chemistry data on vernadite, and by extension the phyllomanganate–water interface (Appelo and Postma, 1999; Tonkin et al., 2004).

APPENDIX A. SUPPLEMENTARY DATA

Supplementary data associated with this article can be found, in the online version, at http://dx.doi.org/10.1016/j.gca.2012.02.019.

REFERENCES

Aplin A. C. and Cronan D. S. (1985) Ferromanganese oxide deposits from the Central Pacific Ocean, I. Encrustations from the Line Islands Archipelago. *Geochim. Cosmochim. Acta* **49**, 427–436.

Appelo C. A. J. and Postma D. (1999) A consistent model for surface complexation on birnessite (δ-MnO_2) and its application to a column experiment. *Geochim. Cosmochim. Acta* **63**, 3039–3048.

Banerjee R., Roy S., Dasgupta S., Mukhopadhyay S. and Miura H. (1999) Petrogenesis of ferromanganese nodules from east of the Chagos Archipelago, Central Indian Basin, Indian Ocean. *Mar. Geol.* **157**, 145–158.

Bargar J. R., Fuller C. C., Marcus M. A., Brearley A. J., Perez De la Rosa M., Webb S. M. and Caldwell W. A. (2009) Structural characterization of terrestrial microbial Mn oxides from Pinal Creek, AZ. *Geochim. Cosmochim. Acta* **73**, 889–910.

Bodeï S., Manceau A., Geoffroy N., Baronnet A. and Buatier M. (2007) Formation of todorokite from vernadite in Ni-rich hemipelagic sediments. *Geochim. Cosmochim. Acta* **71**, 5698–5716.

Bogdanov Y. A., Gurvich E. G., Bogdanova O. Y., Ivanov G. V., Isaeva A. B., Murav'ev K. G., Gorshkov A. I. and Dubinina G. I. (1995) Ferromanganese nodules of the Kara Sea. *Okeanologiya* **34**, 722–732.

Boonfueng T., Axe L., Yee N., Hahn D. and Ndiba P. K. (2006) Zn sorption mechanisms onto sheathed *Leptothrix discophora* and the impact of the nanoparticulate biogenic Mn oxide coating. *J. Coll. Interf. Sci.* **333**, 439–447.

Boonfueng T., Axe L., Yee N., Hahn D. and Ndiba P. K. (2009) Zn sorption mechanisms onto sheathed *Leptothrix discophora*and the impact of the nanoparticulate biogenic Mn oxide coating. *J. Coll. Interf. Sci.* **333**, 439–447.

Chukhrov F. V., Sakharov B. A., Gorshkov A. I., Drits V. A. and Dikov Y. P. (1985) Crystal structure of birnessite from the Pacific ocean. *Int. Geol. Rev.* **27**, 1082–1088.

Crerar D. A. and Barnes H. L. (1974) Deposition of deep-sea manganese nodules. *Geochim. Cosmochim. Acta* **38**, 279–300.

Dorn R. I. and Oberlander T. M. (1981) Microbial origin of desert varnish. *Science* **213**, 1245–1247.

Dorn R. I., Krinsley D. H., Liu T., Anderson S., Clark J., Cahill T. A. and Gill T. E. (1992) Manganese-rich rock varnish does occur in Antarctica. *Chem. Geol.* **99**, 289–298.

Drits V. A. and Tchoubar C. (1990) *X-ray Diffraction by Disordered Lamellar Structures: Theory and Applications to Microdivided Silicates and Carbons*. Springer-Verlag, Berlin.

Drits V. A., Silvester E., Gorshkov A. I. and Manceau A. (1997) Structure of synthetic monoclinic Na-rich birnessite and hexagonal birnessite; I, Results from X-ray diffraction and selected-area electron diffraction. *Am. Mineral.* **82**, 946–961.

Drits V. A., Lanson B., Gorshkov A. I. and Manceau A. (1998) Substructure and superstructure of four-layer Ca-exchanged birnessite. *Am. Mineral.* **83**, 97–118.

Drits V. A., Lanson B., Bougerol-Chaillout C., Gorshkov A. I. and Manceau A. (2002) Structure of heavy-metal sorbed birnessite: Part 2. Results from electron diffraction. *Am. Mineral.* **87**, 1646–1661.

Drits V. A., Lanson B. and Gaillot A.-C. (2007) Birnessite polytype systematics and identification by powder X-ray diffraction. *Am. Mineral.* **92**, 771–788.

Duff M. C., Hunter D. B., Triay I. R., Bertsch P. M., Reed D. T., Sutton S. R., Shea-McCarthy G., Kitten J., Eng P., Chipera S. J. and Vaniman D. T. (1999) Mineral associations and average oxidation states of sorbed Pu on tuff. *Environ. Sci. Technol.* **33**, 2163–2169.

Exon N. F., Raven M. D. and De Carlo E. H. (2002) Ferromanganese nodules and crusts from the Christmas Island Region, Indian Ocean. *Mar. Georesour. Geotec.* **20**, 275–297.

Feng Q., Miyai Y., Kanoh H. and Ooi K. (1992) Li$^+$ extraction/insertion with spinel-type lithium manganese oxides. Characterization of redox-type and ion-exchange-type sites. *Langmuir* **8**, 1861–1867.

Friedl G., Wehrli B. and Manceau A. (1997) Solid phases in the cycling of manganese in eutrophic lakes: new insights from EXAFS spectroscopy. *Geochim. Cosmochim. Acta* **61**, 275–290.

Freeman D. S. and Chapman W. G. (1971) An improved oxalate method for the determination of active oxygen in manganese dioxide. *Analyst* **96**, 865–869.

Fuller C. C. and Harvey J. W. (2000) Reactive uptake of trace metals in the hyporheic zone of a mining-contaminated stream, Pinal Creek, Arizona. *Environ. Sci. Technol.* **34**, 1150–1155.

Gaillot A. -C. (2002) *Caractérisation structurale de la birnessite: Influence du protocole de synthèse*. Ph. D. thesis, Université Joseph Fourier – Grenoble1. Available from: <http://tel.arc-hives-ouvertes.fr/docs/00/04/64/67/PDF/tel-00005304.pdf>.

Gaillot A.-C., Lanson B. and Drits V. A. (2005) Structure of birnessite obtained from decomposition of permanganate under soft hydrothermal conditions. 1. Chemical and structural evolution as a function of temperature. *Chem. Mater.* **17**, 2959–2975.

Gaillot A.-C., Drits V. A., Manceau A. and Lanson B. (2007) Structure of the synthetic K-rich phyllomanganate birnessite obtained by high-temperature decomposition of KMnO$_4$: Substructures of K-rich birnessite from 1000 °C experiment. *Micropor. Mesopor. Mater.* **98**, 267–282.

Giovanoli R. (1969) A simplified scheme for polymorphism in the manganese dioxides. *Chimia* **23**, 470–472.

Giovanoli R. (1980) Vernadite is random-stacked birnessite. *Miner. Deposita* **15**, 251–253.

Grangeon S., Lanson B., Lanson M. and Manceau A. (2008) Crystal structure of Ni-sorbed synthetic vernadite: a powder X-ray diffraction study. *Mineral. Mag.* **72**, 1197–1209.

Grangeon S., Lanson B., Miyata N., Tani Y. and Manceau A. (2010) Structure of nanocristalline phyllomanganates produced by freshwater fungi. *Am. Mineral.* **95**, 1608–1616.

He J., Zhang L., Jin S., Zhu Y. and Liu F. (2008) Bacterial communities inside and surrounding soil iron-manganese nodules. *Geomicrobiol. J.* **25**, 14–24.

Hochella, Jr., M. F., Kasama T., Putnis A., Putnis C. V. and Moore J. N. (2005a) Environmentally important, poorly crystalline Fe/Mn hydrous oxides: ferrihydrite and a possibly new vernadite-like mineral from the Clark Fork River Super-fund Complex. *Am. Mineral.* **90**, 718–724.

Hochella, Jr., M. F., Moore J. N., Putnis C. V., Putnis A., Kasama T. and Eberl D. D. (2005b) Direct observation of heavy metal-mineral association from the Clark Fork River Superfund Complex: implications for metal transport and bioavailability. *Geochim. Cosmochim. Acta* **69**, 1651–1663.

Howard S. A. and Preston K. D. (1989) Profile fitting of powder diffraction patterns. In *Modern Powder Diffraction* (eds. D.L. Bish and J.E. Post). Reviews in Mineralogy and Geochemistry 20. Mineralogical Society of America, Chantilly, Va. pp. 217–275.

Isaure M.-P., Laboudigue A., Manceau A., Sarret G., Tiffreau C., Trocellier P., Lamble G., Hazemann J.-L. and Chateigner D. (2002) Quantitative Zn speciation in a contaminated dredged sediment by μ-PIXE, μ-SXRF, EXAFS spectroscopy and principal component analysis. *Geochim. Cosmochim. Acta* **66**, 1549–1567.

Isaure M.-P., Manceau A., Geoffroy N., Laboudigue A., Tamura N. and Marcus M. A. (2005) Zinc mobility and speciation in soil covered by contaminated dredged sediment using micrometer-scale and bulk-averaging X-ray fluorescence, absorption and diffraction techniques. *Geochim. Cosmochim. Acta* **69**, 1173–1198.

Jurgensen A., Widmeyer J. R., Gordon R. A., Bendell-Young L. I., Moore M. M. and Crozier E. D. (2004) The structure of the manganese oxide on the sheath of the bacterium *Leptothrix discophora*: an XAFS study. *Am. Mineral.* **89**, 1110–1118.

Koschinsky A. and Halbach P. (1995) Sequential leaching of marine ferromanganese precipitates: genetic implications. *Geochim. Cosmochim. Acta* **59**, 5113–5132.

Koschinsky A. and Hein J. R. (2003) Uptake of elements from seawater by ferromanganese crusts: solid-phase associations and seawater speciation. *Mar. Geol.* **198**, 331–351.

Kwon K. D., Refson K. and Sposito G. (2009a) On the role of Mn(IV) vacancies in the photoreductive dissolution of hexagonal birnessite. *Geochim. Cosmochim. Acta* **73**, 4142–4150.

Kwon K. D., Refson K. and Sposito G. (2009b) Zinc surface complexes on birnessite: a density functional theory study. *Geochim. Cosmochim. Acta* **73**, 1273–1284.

Kwon K. D., Refson K. and Sposito G. (2010) Surface complexation of Pb(II) by hexagonal birnessite nanoparticles. *Geochim. Cosmochim. Acta* **74**, 6731–6740.

Lafferty B. J., Ginder-Vogel M., Zhu M., Livi K. J. T. and Sparks D. L. (2010) Arsenite oxidation by a poorly crystalline manganese-oxide. 2. Results from X-ray absorption spectroscopy and X-ray diffraction. *Environ. Sci. Technol.* **44**, 8467–8472.

Lanson B., Drits V. A., Silvester E. and Manceau A. (2000) Structure of H-exchange hexagonal birnessite and its mechanism of formation from Na-rich monoclinic buserite at low pH. *Am. Mineral.* **85**, 826–838.

Lanson B., Drits V. A., Feng Q. and Manceau A. (2002a) Structure of synthetic Na-birnessite: evidence for a triclinic one-layer unit cell. *Am. Mineral.* **87**, 1662–1671.

Lanson B., Drits V. A., Gaillot A.-C., Silvester E., Plancon A. and Manceau A. (2002b) Structure of heavy-metal sorbed birnessite: Part 1. Results from X-ray diffraction. *Am. Mineral.* **87**, 1631–1645.

Lanson B., Marcus M. A., Fakra S., Panfili F., Geoffroy N. and Manceau A. (2008) Formation of Zn–Ca phyllomanganate nanoparticles in grass roots. *Geochim. Cosmochim. Acta* **72**, 2478–2490.

Lei G. and Boström K. (1995) Mineralogical control on transition metal distributions in marine manganese nodules. *Mar. Geol.* **123**, 253–261.

Li X., Pan G., Qin Y., Hu T., Wu Z. and Xie Y. (2004) EXAFS studies on adsorption-desorption reversibility at manganese oxide-water interfaces. II. Reversible adsorption of zinc on δ-MnO_2. *J. Coll. Interf. Sci.* **271**, 35–40.

Lingane J. J. and Karplus R. (1946) New method for determination of manganese. *Ind. Eng. Chem. Anal. Ed.* **18**, 191–194.

Manceau A. and Charlet L. (1992) X-ray absorption spectroscopic study of the sorption of Cr(III) at the oxide/water interface. I Molecular mechanism of Cr(III) oxidation on Mn oxides. *J. Coll. Interf. Sci.* **148**, 443–458.

Manceau A., Drits V. A., Silvester E., Bartoli C. and Lanson B. (1997) Structural mechanism of Co^{2+} oxidation by the phyllomanganate buserite. *Am. Mineral.* **82**, 1150–1175.

Manceau A., Lanson B., Schlegel M. L., Harge J. C., Musso M., Eybert-Berard L., Hazemann J.-L., Chateigner D. and Lamble G. M. (2000) Quantitative Zn speciation in smelter-contaminated soils by EXAFS spectroscopy. *Am. J. Sci.* **300**, 289–343.

Manceau A., Lanson B. and Drits V. A. (2002a) Structure of heavy metal sorbed birnessite. Part III: Results from powder and polarized extended X-ray absorption fine structure spectroscopy. *Geochim. Cosmochim. Acta* **66**, 2639–2663.

Manceau A., Marcus M. A. and Tamura N. (2002b) Quantitative Speciation of Heavy Metals in Soils and Sediments by Synchrotron X-ray Techniques.In *Applications of Synchrotron Radiation in Low-Temperature Geochemistry and Environmental Sciences* (eds. P. Fenter and N.C. Sturchio). Reviews in Mineralogy and Geochemistry49. Mineralogical Society of America, Chantilly, Va. pp. 341–428.

Manceau A., Tamura N., Celestre R. S., MacDowell A. A., Geoffroy N., Sposito G. and Padmore H. A. (2003) Molecular-scale speciation of Zn and Ni in soil ferromanganese nodules

from Loess soils of the Mississippi Basin. *Environ. Sci. Technol.* **37**, 75–80.

Manceau A., Marcus M. A., Tamura N., Proux O., Geoffroy N. and Lanson B. (2004) Natural speciation of Zn at the micrometer scale in a clayey soil using X-ray fluorescence, absorption, and diffraction. *Geochim. Cosmochim. Acta* **68**, 2467–2483.

Manceau A., Tommaseo C., Rihs S., Geoffroy N., Chateigner D., Schlegel M., Tisserand D., Marcus M. A., Tamura N. and Chen Z. S. (2005) Natural speciation of Mn, Ni and Zn at the micrometer scale in a clayey paddy soil using X-ray fluorescence, absorption, and diffraction. *Geochim. Cosmochim. Acta* **69**, 4007–4034.

Manceau A., Lanson M. and Geoffroy N. (2007a) Natural speciation of Ni, Zn, Ba, and As in ferromanganese coatings on quartz using X-ray fluorescence, absorption, and diffraction. *Geochim. Cosmochim. Acta* **71**, 95–128.

Manceau A., Kersten M., Marcus M. A., Geoffroy N. and Granina L. (2007b) Ba and Ni speciation in a nodule of binary Mn oxide phase composition from Lake Baikal. *Geochim. Cosmochim. Acta* **71**, 1967–1981.

Mandernack K. W., Post J. and Tebo B. M. (1995) Manganese mineral formation by bacterial spores of the marine *Bacillus*, strain SG-1: evidence for the direct oxidation of Mn(II) to Mn(IV). *Geochim. Cosmochim. Acta* **59**, 4393–4408.

Marcus M. A., Manceau A. and Kersten M. (2004a) Mn, Fe, Zn and As speciation in a fast-growing ferromanganese marine nodule. *Geochim. Cosmochim. Acta* **68**, 3125–3136.

Marcus M. A., MacDowell A. A., Celestre R., Manceau A., Miller T., Padmore H. A. and Sublett R. E. (2004b) Beamline 10.3.2 at ALS: a hard X-ray microprobe for environmental and materials sciences. *J. Synchrotron Radiat.* **11**, 239–247.

McKenzie R. M. (1980) The adsorption of lead and other heavy metals on oxides of manganese and iron. *Aust. J. Soil Res.* **18**, 61–73.

McKeown D. A. and Post J. E. (2001) Characterization of manganese oxide mineralogy in rock varnish and dendrites using X-ray absorption spectroscopy. *Am. Mineral.* **86**, 701–713.

Miyata N., Tani Y., Iwahori K. and Soma M. (2004) Enzymatic formation of manganese oxides by an *Acremonium*-like hyphomycete fungus, strain KR21-2. *FEMS Microbiol. Ecol.* **47**, 101–109.

Miyata N., Sugiyama D., Tani Y., Tsuno H., Seyama H., Sakata M. and Iwahori K. (2007) Production of biogenic manganese oxides by repeated-batch cultures of laboratory microcosms. *J. Biosci. Bioeng.* **103**, 432–439.

Morgan J. J. (2005) Kinetics of reaction between O_2 and Mn(II) species in aqueous solutions. *Geochim. Cosmochim. Acta* **69**, 35–48.

Murray J. W., Balistrieri L. S. and Paul B. (1984) The oxidation state of manganese in marine sediments and ferromanganese nodules. *Geochim. Cosmochim. Acta* **48**, 1237–1247.

Nasser A., Buchanovsky N., Gerstl Z. and Mingelgrin U. (2009) Mineral induced mechanochemical degradation: the imazaquin case. *Chemosphere* **75**, 20–27.

Olivie-Lauquet G., Gruau G., Dia A., Riou C., Jaffrezic A. and Henin O. (2001) Release of trace elements in wetlands: role of seasonal variability. *Water Res.* **35**, 943–952.

Ostwald J. and Frazer F. W. (1973) Chemical and mineralogical investigations on deep sea manganese nodules from the Southern Ocean. *Miner. Deposita* **8**, 303–311.

Peacock C. L. and Sherman D. M. (2007) Crystal-chemistry of Ni in marine ferromanganese crusts and nodules. *Am. Mineral.* **92**, 1087–1092.

Peacock C. L. (2009) Physiochemical controls on the crystal-chemistry of Ni in birnessite: genetic implications for ferro-manganese precipitates. *Geochim. Cosmochim. Acta* **73**, 3568–3578.

Peña J., Kwon K. D., Refson K., Bargar J. R. and Sposito G. (2010) Mechanisms of nickel sorption by a bacteriogenic birnessite. *Geochim. Cosmochim. Acta* **74**, 3076–3089.

Peña J., Bargar J. R. and Sposito G. (2011) Role of bacterial biomass in the sorption of Ni by biomass-birnessite assemblages. *Environ. Sci. Technol.* **45**, 7338–7344.

Pizzigallo M. D. R., Napola A., Spagnuolo M. and Ruggiero P. (2004) Mechanochemical removal of organo-chlorinated compounds by inorganic components of soil. *Chemosphere* **55**, 1485–1492.

Post J. E. and Appleman D. E. (1988) Chalcophanite, $ZnMn_3O_7.3-H_2O$; new crystal-structure determinations. *Am. Mineral.* **73**, 1401–1404.

Post J. E. and Appleman D. E. (1994) Crystal structure refinement of lithiophorite. *Am. Mineral.* **79**, 370–374.

Post J. E. and Veblen D. R. (1990) Crystal structure determinations of synthetic sodium, magnesium, and potassium birnessite using TEM and the Rietveld method. *Am. Mineral.* **75**, 477–489.

Santelli C. M., Webb S. M., Dohnalkova A. C. and Hansel C. M. (2011) Diversity of Mn oxides produced by Mn(II)-oxidizing fungi. *Geochim. Cosmochim. Acta* **75**, 2762–2776.

Schulze D. G., McCaybuis T., Sutton S. R. and Huber D. M. (1995) Manganese oxidation-states in *Gaeumannomyces*-infested wheat rhizospheres probed by micro-xanes spectroscopy. *Phytopathology* **85**, 990–994.

Sherman D. M. and Peacock C. L. (2010) Surface complexation of Cu on birnessite (δ-MnO_2): controls on Cu in the deep ocean. *Geochim. Cosmochim. Acta* **74**, 6721–6730.

Silvester E., Charlet L. and Manceau A. (1995) The mechanism of chromium(III) oxidation by Na-buserite. *J. Phys. Chem.* **99**, 16662–16772.

Silvester E., Manceau A. and Drits V. A. (1997) Structure of synthetic monoclinic Na-rich birnessite and hexagonal birnessite; II. Results from chemical studies and EXAFS spectroscopy. *Am. Mineral.* **82**, 962–978.

Stone A. T. and Morgan J. J. (1984a) Reduction and dissolution of manganese(III) and manganese(IV) oxides by organics. 1. Reaction with hydroquinone. *Environ. Sci. Technol.* **18**, 450–456.

Stone A. T. and Morgan J. J. (1984b) Reduction and dissolution of manganese(III) and manganese(IV) oxides by organics: 2. Survey of the reactivity of organics. *Environ. Sci. Technol.* **18**, 617–624.

Sunda W. G. and Kieber D. J. (1994) Oxidation of humic substances by manganese oxides yields low-molecular-weight organic substrates. *Nature* **367**, 62–64.

Takahashi Y., Manceau A., Geoffroy N., Marcus M. A. and Usui A. (2007) Chemical and structural control of the partitioning of Co, Ce, and Pb in marine ferromanganese oxides. *Geochim. Cosmochim. Acta* **71**, 984–1008.

Tani Y., Miyata N., Iwahori K., Soma M., Tokuda S.-I., Seyama H. and Theng B. K. G. (2003) Biogeochemistry of manganese oxide coatings on pebble surfaces in the Kikukawa River System, Shizuoka, Japan. *Appl. Geochem.* **18**, 1541–1554.

Tebo B. M., Bargar J. R., Clement B. G., Dick G. J., Murray K. J., Parker D., Verity R. and Webb S. M. (2004) Biogenic manganese oxides: properties and mechanisms of formation. *Annu. Rev. Earth Planet. Sci.* **32**, 287–328.

Toner B., Fakra S., Villalobos M., Warwick T. and Sposito G. (2005) Spatially resolved characterization of biogenic manganese oxide production within a bacterial biofilm. *Appl. Environ. Microbiol.* **71**, 1300–1310.

Toner B., Manceau A., Webb S. M. and Sposito G. (2006) Zinc sorption to biogenic hexagonal-birnessite particles within a hydrated bacterial biofilm. *Geochim. Cosmochim. Acta* **70**, 27–43.

Tonkin J. W., Balistrieri L. S. and Murray J. W. (2004) Modeling sorption of divalent metal cations on hydrous manganese oxide using the diffuse double layer model. *Appl. Geochem.* **19**, 29–53.

Vaněk A., Ettler V., Grygar T., Borůvka L., Šebek O. and Drábek O. (2008) Combined chemical and mineralogical evidence for heavy metal binding in mining- and smelting-affected alluvial soils. *Pedosphere* **18**, 464–478.

Vetter K. J. and Jaeger N. (1966) Potentialausbildung an der mangandioxid-elektrode als oxidelektrode mit nichtstochiometrischemoxid. *Electrochim. Acta* **11**, 401–419.

Villalobos M., Toner B., Bargar J. and Sposito G. (2003) Characterization of the manganese oxide produced by *Pseudomonas putida* strain MnB1. *Geochim. Cosmochim. Acta* **67**, 2649–2662.

Villalobos M., Bargar J. R. and Sposito G. (2005) Mechanisms of Pb(II) sorption on a biogenic manganese oxide. *Environ. Sci. Technol.* **39**, 569–576.

Villalobos M., Lanson B., Manceau A., Toner B. and Sposito G. (2006) Structural model for the biogenic Mn oxide produced by *Pseudomonas putida*. *Am. Mineral.* **91**, 489–502.

Villatoro-Monzón W. R., Mesta-Howard A. M. and Razo-Flores E. (2003) Anaerobic biodegradation of BTEX using Mn(IV) and Fe(III) as alternative electron acceptors. *Water Sci. Technol.* **48**, 125–131.

Wadsley A. (1955) The crystal structure of chalcophanite, $ZnMn_3O_7.3H_2O$. *Acta Cryst.* **8**, 165–172.

Webb S. M., Tebo B. M. and Bargar J. R. (2005) Structural characterization of biogenic Mn oxides produced in seawater by the marine *Bacillus sp.* strain SG-1. *Am. Mineral.* **90**, 1342–1357.

Webster R. (2001) Statistics to support soil research and their presentation. *Eur. J. Soil Sci.* **52**, 331–340.

Zhao W., Cui H., Liu F., Tan W. and Feng X. H. (2009) Relationship between Pb^{2+} adsorption and average Mn oxidation state in synthetic birnessite. *Clays Clay Miner.* **57**, 513–520.

Zhu M., Ginder-Vogel M., Parikh S. J., Feng X. H. and Sparks D. L. (2010a) Cation effects on the layer structure of biogenic Mn-oxides. *Environ. Sci. Technol.* **44**, 4465–4471.

Zhu M., Ginder-Vogel M., Parikh S. J., Feng X. H. and Sparks D. L. (2010b) Ni(II) sorption on biogenic Mn-oxides with varying Mn octahedral layer structure. *Environ. Sci. Technol.* **44**, 4472–4478.

Associate editor: Jon Chorover

Electronic Annex

to the article "Zn sorption modifies dynamically the layer and interlayer structure of vernadite" authored by Sylvain Grangeon, Alain Manceau, Julien Guilhermet, Anne-Claire Gaillot, Martine Lanson & Bruno Lanson

Potentiometric titration of Mn oxidation state with $(NH_4)_2FeSO_4$ (Mohr salt) and $Na_4P_2O_7$

Preliminary step: solution preparation

All solutions are prepared using analytical grade chemicals and deionized water (DI) with a resistivity of > 18 MΩ/cm. DI water is boiled and degassed with argon gas for ~30 minutes, then cooled under constant Ar bubbling prior to be used for solution preparation.

Potassium permanganate ($KMnO_4$) solution
A 0.02 M (3.1606 g/L) solution of $KMnO_4$ is prepared and kept in the dark for several days before being filtered at 0.1 μm and used.

Mohr salt $(NH_4)_2Fe(SO_4)_2 \bullet 6H_2O$ solution
A solution with a concentration of ~3.9 g/L is prepared in acidified water (10wt% H_2SO_4). This solution is redox sensitive and should be prepared just before use. It may be kept in the fridge between two experiments, but no longer than half a day.

Step 1: Titration of the Mohr salt solution with $KMnO_4$
50 mL of the Mohr salt solution are titrated with the $KMnO_4$ solution. This step aims at determining the concentration of Fe^{2+} ions in the Mohr salt solution. Titration is potentiometric, and solution redox is thus monitored after each addition step. Equivalence is reached when a drop of $KMnO_4$ induces a significant jump of the solution redox (from ~0.8 to ~1.5 V).

Redox couples are:
$KMnO_4/Mn^{2+}$ $\qquad$ $E_0 = 1.507$ V
Fe^{3+}/Fe^{2+} $\qquad$ $E_0 = 0.771$ V

And corresponding reactions are:
$MnO_4^- + 8 H^+ + 5 e^-$ $\qquad$ $\Leftrightarrow Mn^{2+} + 4 H_2O$
$5 Fe^{2+}$ $\qquad$ $\Leftrightarrow 5 Fe^{3+} + 5 e^-$

$MnO_4^- + 8 H^+ + 5 Fe^{2+}$ $\qquad$ $\Leftrightarrow Mn^{2+} + 4 H_2O + 5 Fe^{3+}$

From this equation,

$n(Fe_{tot}) = 5\, n(MnO_4^-)$, and thus $n(Fe_{tot}) = 5C \times V_0$ (1)

With $n(MnO_4^-)$ and $n(Fe_{tot})$ the numbers of permanganate and iron moles in the two solutions; C and V_0 the concentration of the permanganate solution and the volume at the equivalence point, respectively.

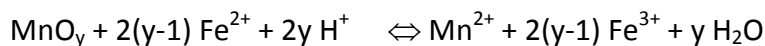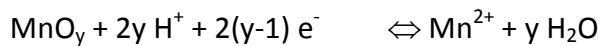## Step 2: Reduction of the manganese oxide using Fe^{2+}

20 to 30 mg of the manganese oxide are added to 50 mL of the Mohr salt solution before its titration. The volume of the Mohr salt solution must be strictly identical to that in step 1. The manganese oxide should be dispersed in the Mohr salt solution to promote reductive dissolution of the Mn oxide. If shaking is not sufficient for this purpose it is recommended to use ultrasonic dispersion. In this case, dispersion should be performed in the dark to minimize oxidation of the Mohr salt solution, and special attention should be paid to avoid heating the solution. No Mn oxide grains should be present before titration of this solution with $KMnO_4$.

Redox couples for the reductive dissolution are:

MnO_x/Mn^{2+} $E_0 = 1.224$ V (for MnO2)
Fe^{3+}/Fe^{2+} $E_0 = 0.771$ V

And the corresponding reactions:

$MnO_y + 2y\, H^+ + 2(y-1)\, e^-$ $\Leftrightarrow Mn^{2+} + y\, H_2O$
$2(y-1)\, Fe^{2+}$ $\Leftrightarrow 2(y-1)\, Fe^{3+} + 2(y-1)\, e^-$

$MnO_y + 2(y-1)\, Fe^{2+} + 2y\, H^+$ $\Leftrightarrow Mn^{2+} + 2(y-1)\, Fe^{3+} + y\, H_2O$

From this equation,

$2(y-1)\, n(Mn) = 2(y-1)\, n(MnO_y) = n(Fe_{reacted}) = n(Fe_{tot}) - n(Fe_{excess})$ (2)

With n the number of moles of the different species.

Redox couples for the titration of excess Fe^{2+} are the same as those in step 1, V_1 being the volume of the permanganate solution at the equivalence point.

As a consequence:

$n(Fe_{excess}) = 5\, n(MnO_4^-)_{titr}$, and thus $n(Fe_{excess}) = 5C \times V_1$ (3)
and $2(y-1)\, n(MnO_x) = 5C \times V_0 - 5C \times V_1 = 5C \times (V_0 - V_1)$ (4)

To minimize uncertainties, steps 1 and 2 must be performed simultaneously using identical experimental conditions to both solutions. Thus, solutions from step 1 and step 2 should be prepared at the same time, and both solutions should undergo the same protocol. In
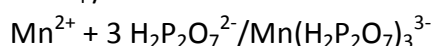
particular, this allows avoiding uncertainties linked to the evolution of Fe^{2+} concentration in Mohr salt solution.

Step 3: Back-titration of Fe^{2+} in excess after step 2.

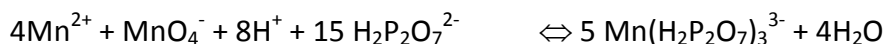In a beaker, 8 to 10 grams of sodium pyrophosphate ($Na_4P_2O_7$) should be mixed with ~0.1 L of DI water to prepare a solution supersaturated with respect to pyrophosphate. This solution is then mixed with the one obtained at the end of step 2 (after titration), and pH is adjusted to 6.5-6.6 with concentrated H_2SO_4 to maximize the amplitude of the potential change at the equivalence point. Special attention should be paid to use the whole volume of solution obtained at the end of step 2.

The resulting solution is then titrated potentiometrically with $KMnO_4$ to determine the amount of Mn^{2+} formed during step 2.

Redox couples are:

MnO_4^-/Mn^{2+} $\qquad\qquad\qquad\qquad$ $E_0 = 1.507$ V

$Mn^{2+} + 3\ H_2P_2O_7^{2-}/Mn(H_2P_2O_7)_3^{3-}$

And corresponding reactions are:

$MnO_4^- + 8H^+ + 5e^-$ $\qquad\qquad\qquad$ $\Leftrightarrow Mn^{2+} + 4H_2O$

$5Mn^{2+} + 15\ H_2P_2O_7^{2-}$ $\qquad\qquad\qquad$ $\Leftrightarrow 5\ Mn(H_2P_2O_7)_3^{3-} + 5e-$

$4Mn^{2+} + MnO_4^- + 8H^+ + 15\ H_2P_2O_7^{2-}$ $\qquad$ $\Leftrightarrow 5\ Mn(H_2P_2O_7)_3^{3-} + 4H_2O$

From this equation,

$n(Mn^{2+}) = 4\ n(MnO_4^-) = 4C \times V_2$ $\hfill$ (5)

With n the number of moles of the different species, V_2 being the volume of $KMnO_4$ solution at the equivalence point.

In addition:

$n(Mn^{2+}) = n(MnO_y) + n(MnO_4^-)_{titr}$ $\hfill$ (6)

Combining Equations (3), (5), and (6) one may deduce:

$n(MnO_y) = 4C \times V_2 - C \times V_1$ $\hfill$ (7)

Combining Equations (4) and (7) one may deduce:

$5C \times (V0 - V1) / 2(y -1) = C \times (4V_2 - V_1)$ $\hfill$ (8)

And finally:

$2y = 2 + 5 \times (V_0 - V_1) / (4V_2 - V_1)$ $\hfill$ (9)

2y being the average oxidation degree of manganese in the Mn oxide.

Using this titration protocol, it is not necessary to determine accurately the solution concentrations, nor the volume of the Mohr salt solution. All volumes at equivalence points can be determined accurately using potentiometric titrations, and the only source of error is the reproducibility of the volumes of Mohr salt solution used for the first two steps of the titration. No additional analytical or dilution error is to be considered.